Supporting Information

A Striking Interfacial Interaction between Cu_2O and Black Phosphorus Boosts Solar-to-Hydrogen Conversion

Giacomo Provinciali[1], Manuel Serrano-Ruiz[1], Jonathan Filippi[1], Beatrice Muzzi[1], Martina Banchelli[2], Stefano Caporali[3], Maurizio Peruzzini[1], Giovanni Barcaro[4], Susanna Monti[5], Maria Caporali[1*]

[1] Institute of Chemistry of OrganoMetallic Compounds, National Council for Research, CNR-ICCOM, Via Madonna del Piano 10, I-50019 Sesto Fiorentino, Italy.

[2] Institute of Applied Physics "Nello Carrara", National Council for Research, CNR-IFAC, Via Madonna del Piano 10, 50019 Sesto Fiorentino, Italy.

[3] Department of Industrial Engineering, University of Florence, Via di S. Marta 3, 50139 Firenze, Italy.

[4] Institute of Chemical and Physical Processes, National Council for Research, CNR-IPCF, via G. Moruzzi 1, I-56124 Pisa, Italy.

[5] Institute of Chemistry of OrganoMetallic Compounds, National Council for Research, CNR-ICCOM, via G. Moruzzi 1, I-56124 Pisa, Italy.

Characterization of the nanomaterials

SEM microscopy. Scanning Electron Microscopy experiments were carried out at Ce.ME CNR (Sesto Fiorentino, Italy) using a Dual Beam, TESCAN GAIA3 FIB/SEM ultrahigh resolution field emission microscope at 5 KeV voltage. The samples were suspended in acetone by ultrasonication and drop-cast on a carbon/copper grid, dried under a stream of nitrogen and measured right after.

High Resolution TEM microscopy. HRTEM images were acquired using a Thermofisher Talos F200X G2 at an accelerating voltage of 200 kV and a camera resolution of 4096 x 4096 pixels without a lens aperture. High Angle Annular Dark Field (HAADF) images were acquired with an annular STEM detector using a convergent beam with an angle of 10.5 mrad. EDX maps were taken with a Super X spectrometer equipped with four 30 mm^2 silicon drift detectors for a collection angle of 0.7 srad.

X-ray diffraction (XRD). Data were collected on the powder samples with an X'Pert PRO diffractometer, operating in Bragg-Brentano parafocusing geometry with a Cu target and Kα radiation (λ = 1.5418) at 40 kV beam voltage and 40 mA current. The data were collected in the 5°-90° 2θ range, with steps of 0.01° and a counting time of 130 s.

Raman. Raman characterization of the samples was performed at room temperature in a backscattering configuration using a LabRam HR 800EVO Raman spectrometer (Horiba France SAS) equipped with an Olympus BXFM microscope (objective X100, NA 0.9), TE-cooled CCD detector (Syncerity OE), 633 nm HeNe laser, and 600 grooves/mm diffraction grating. The spectral resolution was 0.9-1.8 cm^{-1}. The sample was drop-cast on silicon wafers as the substrate, then it was dried in a nitrogen atmosphere. The laser power at the sample was 0.7 mW, and the acquisition time was 1 s. Ten to twenty spectra were registered for each sample at different locations to verify sample homogeneity and the absence of photoinduced phenomena. The reference spectrum of Si was measured contextually in each sample. Raman spectra were corrected for the baseline, and the peak analysis was performed through the Lorentzian fitting function to calculate the position, intensity, and area of the characteristic peaks.

UV-Vis DRS. The UV-Vis absorption and diffuse reflectance spectra were measured on the solid samples with a Shimadzu UV-2600 spectrometer using an integrating sphere with $BaSO_4$ as a reference material. By using the Kubelka-Munk equation, Tauc plots were obtained, and the optical band-gap energy of the samples was extrapolated.

XPS. X-ray Photoelectron Spectroscopy (XPS) measurements were performed at the Chemistry Department, University of Florence (Italy) in an ultra-high vacuum (10^{-9} mbar) system equipped with a VSW HAC 5000 hemispherical electron energy analyzer and a non-monochromatized Mg-Kα X-ray source (1253.6 eV). The source power used was 100 W (10 kV×10 mA), and the spectra were acquired in the constant-pass-energy mode at E_{pas} = 44 eV. The overall energy resolution was 1.2 eV as a full-width at half maximum (FWHM) for the Ag $3d_{5/2}$ line of a pure silver reference. The recorded spectra were fitted using XPS Peak 4.1 software employing Gauss-Lorentz curves after subtraction of a Shirley-type background. The samples were drop-cast from a suspension in methanol, dried under a stream of nitrogen, and introduced into the UHV system via a loadlock under inert gas (N2) flux, in order to minimize the exposure to air contaminants and kept in the introduction chamber for at least 12 hours before the measurements.

Photocatalytic H_2 production

The photocatalytic hydrogen evolution experiments were performed in a 30 mL cylindrical quartz reactor at ambient temperature (T = 25°C). 1.3 mg of catalyst was ultrasonically dispersed in 3 mL of degassed MilliQ water solution containing the desired amount of methanol (V_{H2O}: V_{MeOH} = 4), and the reactor was closed with a rubber cap equipped with a silicone septum. A 300-Watt Xe lamp (mKs-Newport) was used as the light source. The stirring was started when the light was irradiated on the sample. The measurements were carried out by irradiating in the UV-Vis region or in the full spectrum UV-Vis-IR. Before irradiation, nitrogen gas was bubbled for 30 min to remove the air inside. The evolved hydrogen gas was sampled every hour and determined using an off-line gas chromatograph (Shimadzu GC-2010) equipped with a thermal conductivity detector (TCD) and a 5 Å molecular sieve column.

Analysis of hydroxyl radicals

1.3 mg of catalyst was ultrasonically dispersed in 2.65 mL of degassed MilliQ water solution containing the desired amount of methanol (V_{H2O}: V_{MeOH} = 4) and 0.35 mL of coumarin aqueous solution (0.0025 M), keeping an inert atmosphere. The reactor was closed and irradiated under stirring for two hours by using a 300-Watt Xe lamp (mKs-Newport) in the full spectrum UV-Vis-IR. A sample was taken and the photoluminescence was measured applying a λexc = 350 nm.

Electrochemical measurements

Electrochemical measurements, including electrochemical impedance spectra (EIS) and specific capacitance performances (cyclic voltammetry, CV), were carried out in a standard three-electrode cell on an electrochemical workstation (PARSTAT 2273 potentiostat). The EIS (perturbation voltage 20 mV, frequency 110 KHz – 100 mHz) and CV were measured using an Ag/AgCl electrode as the reference electrode, a platinum plate as the counter electrode, and 0.5 M Na_2SO_4 aqueous solution as the electrolyte. To prepare the working electrode, pristine TiO_2, the as-synthesized Cu_2O, $TiO_2/BP_{1\%}$, $TiO_2/Cu_2O_{5\%}$ and TiO_2/BP-Cu_2O nanocomposites were first dispersed in MeOH (1.0 mL). The dispersion containing the catalyst (3.0 mg/mL) was deposited by drop-coating on a fluorine-doped tin oxide (FTO) conductive glass substrate (2.0 cm^2) and was dried under a stream of nitrogen before measurements. Mott-Schottky (M-S) curves were measured under an arc amplitude of 10 mV and frequency of 1 kHz.

Photoluminescence

PL measurements were registered using a Jasco spectrofluorometer model FP-8300. The powder samples TiO_2, TiO_2/BP(1%), TiO_2/Cu_2O(5%), and TiO_2/BP(1%)-Cu_2O(5%) were analysed by irradiating at a wavelength close to the maximum absorption in the corresponding UV-Vis spectrum, i.e., λ = 325 nm.

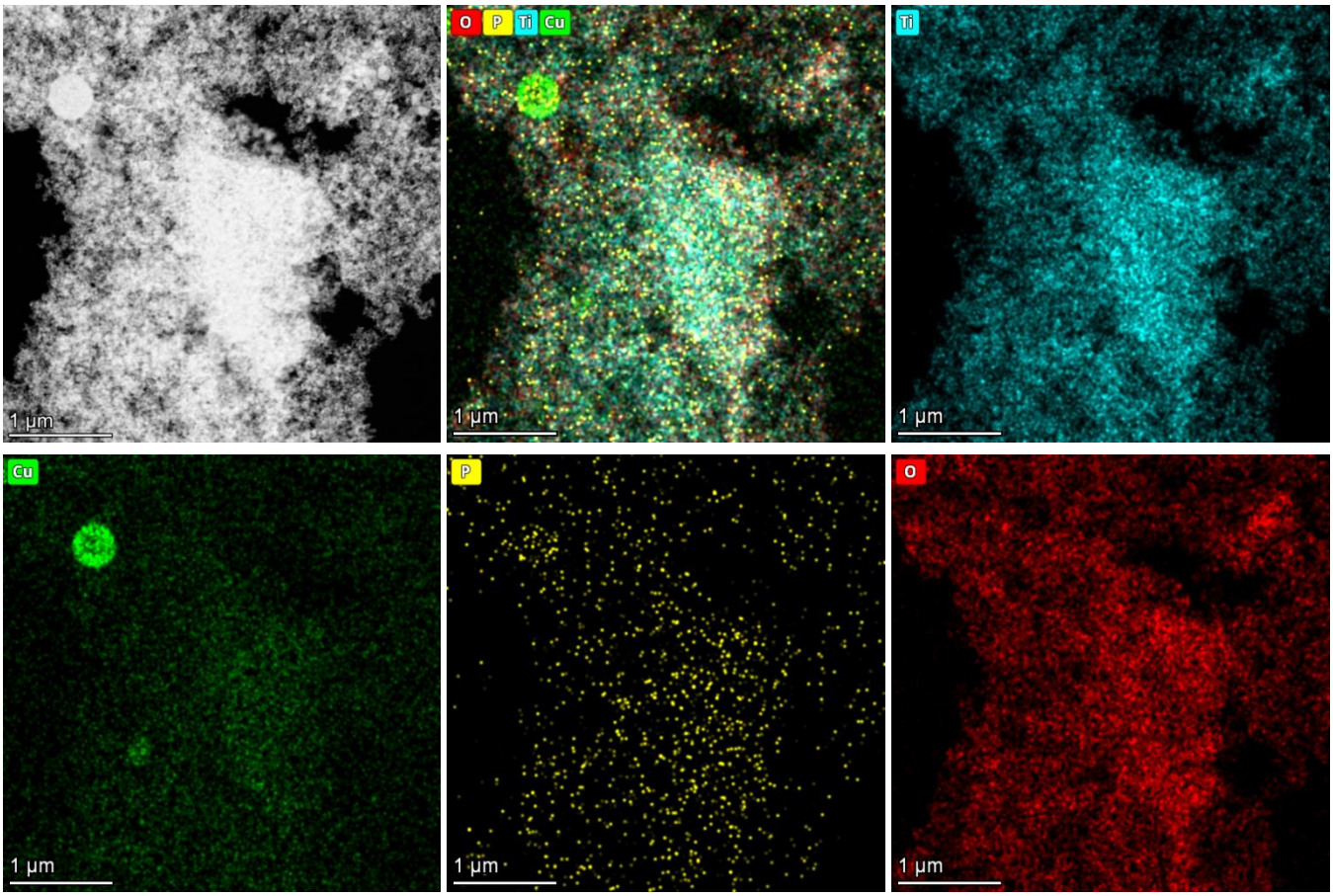

Figure S1. STEM HAADF image of $TiO_2/(Cu_2O\text{-}BP)_{6\%}$ with the corresponding elements' distribution maps, obtained by EDX analysis.

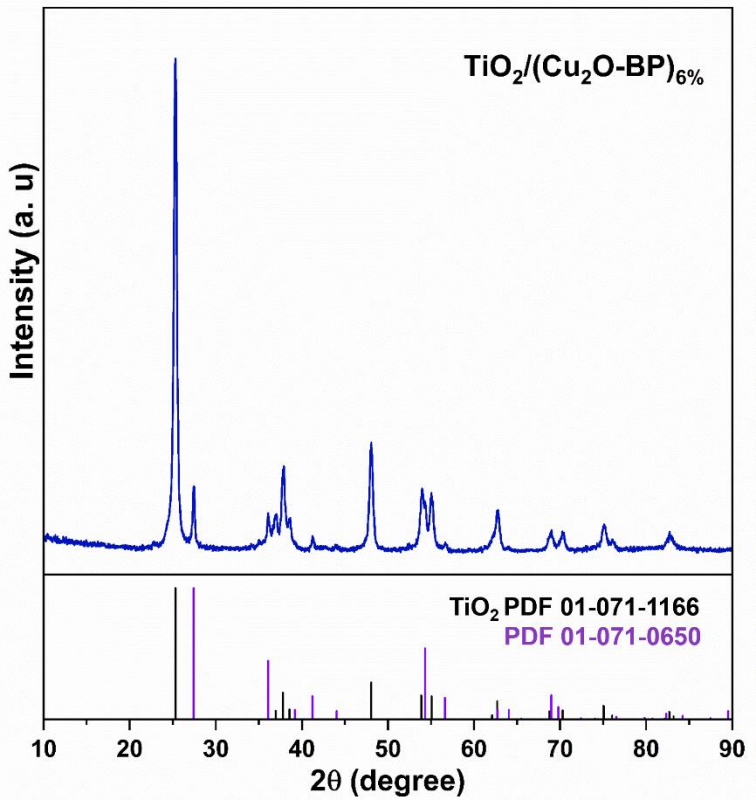

Figure S2. PXRD of $TiO_2/(Cu_2O\text{-}BP)_{6\%}$.

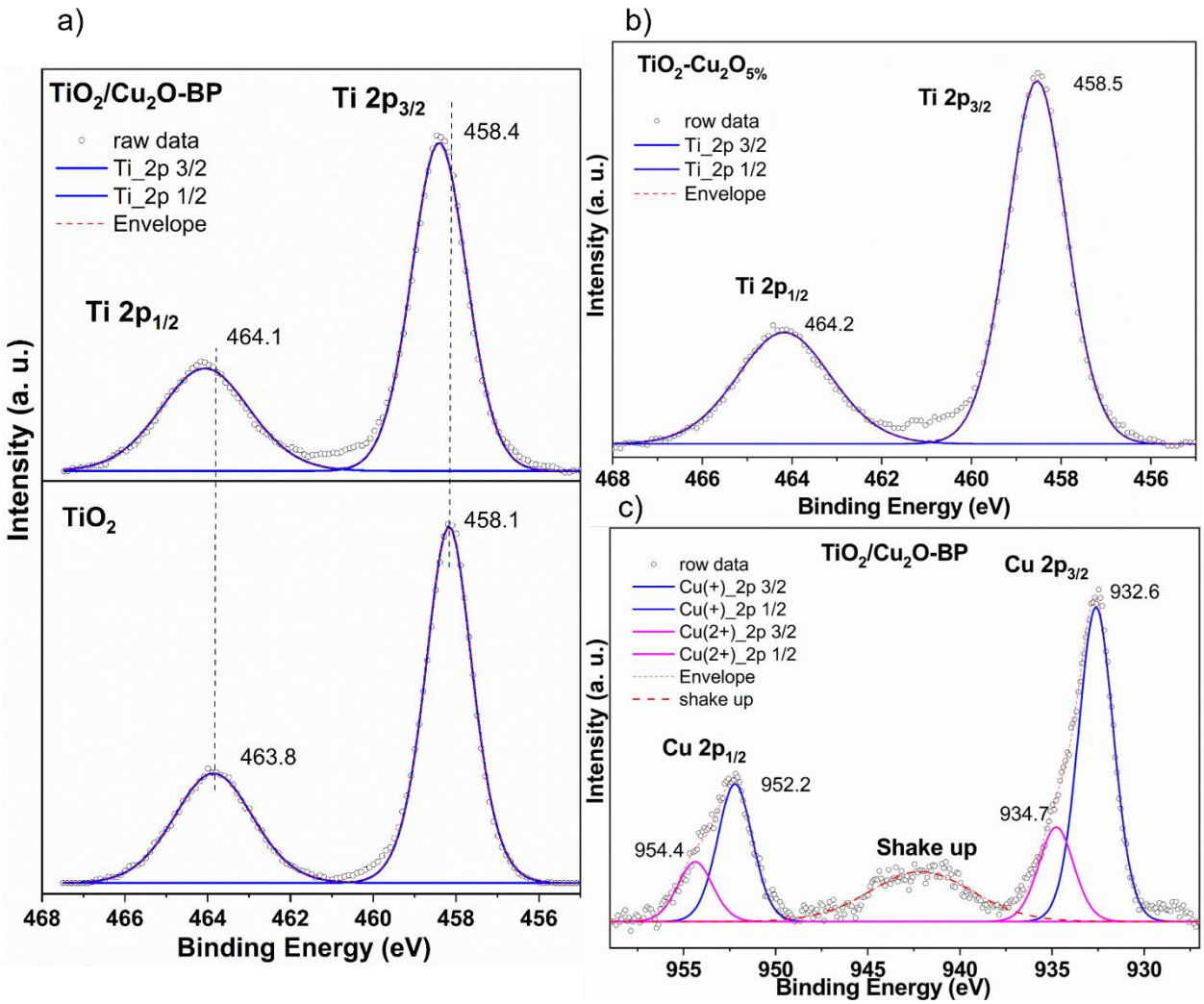

Figure S3. a) Core level Ti 2p XPS spectra of TiO_2 (bottom) and TiO_2/Cu_2O(5%)-BP(1%) (up); b) Core level Ti 2p XPS spectrum of TiO_2/Cu_2O(5%); c) Core level Cu 2p XPS spectrum of the ternary $TiO_2/(Cu_2O\text{-}BP)_{6\%}$.

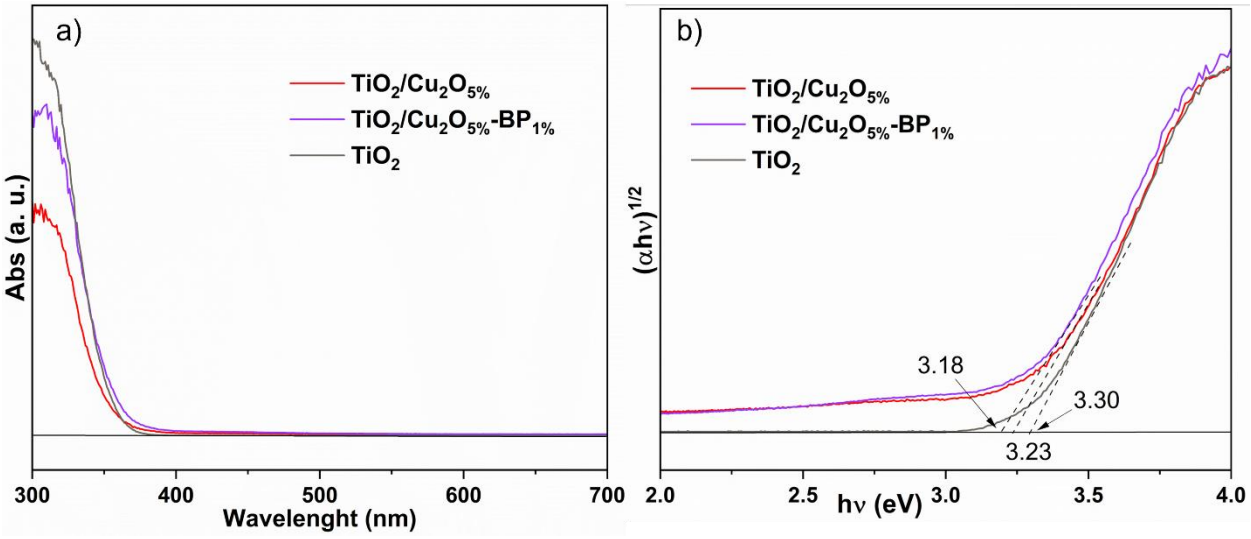

Figure S4. a) UV-Vis spectra and b) Tauc plot of pure TiO_2, $TiO_2/Cu_2O_{5\%}$ and $TiO_2/BP_{1\%}$-$Cu_2O_{5\%}$

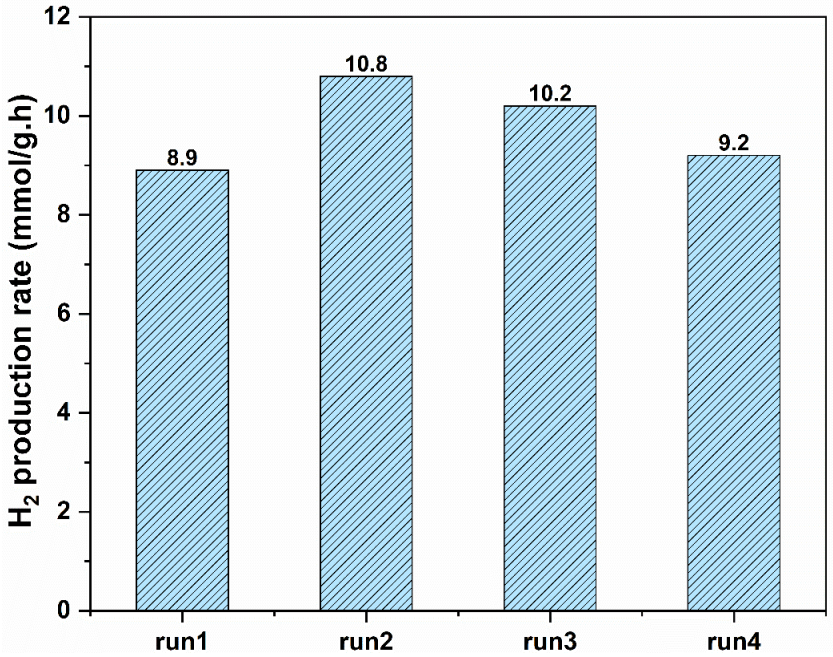

Figure S5. Cycling stability of the photocatalyst $TiO_2/BP_{1\%}$-$Cu_2O_{2\%}$. H_2 gas was sampled every 50 minutes and each run last 150 minutes. The values shown in the graph are the average of each run.

Table S1. ICP analysis on the filtrate after four consecutive catalytic run.

Phosphorus	mg/L	0.10± 0.05
Copper	µg/L	0.24

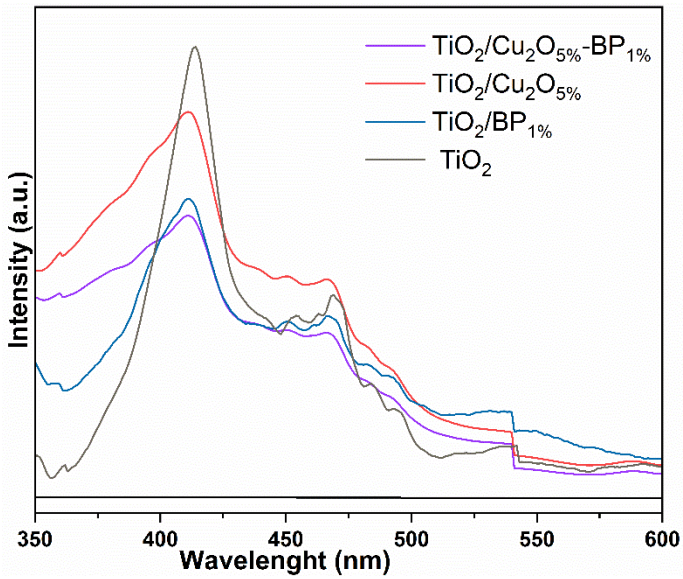

Figure S6. Photoluminescence spectra of pure TiO_2 and of the corresponding nanocomposites.

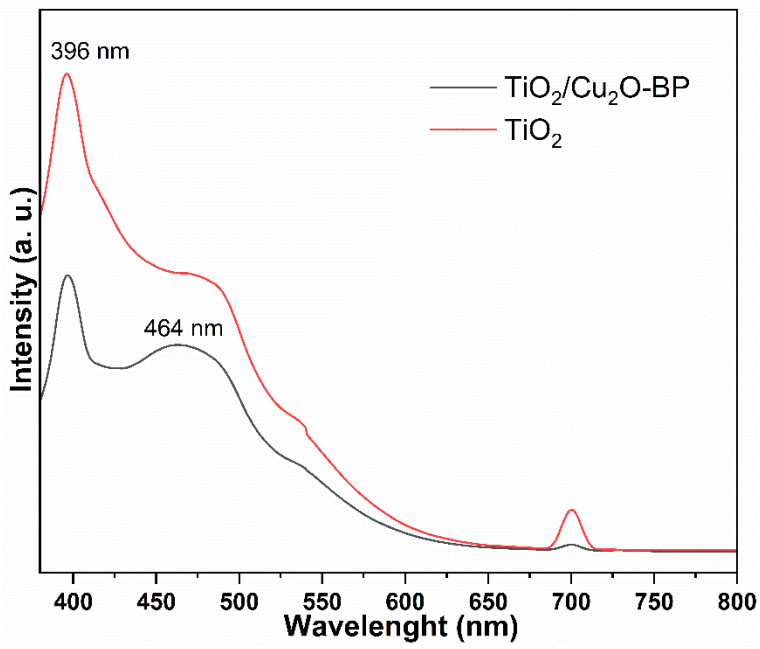

Figure S7. Photoluminescence spectra of $TiO_2/(Cu_2O\text{-}BP)_{6\%}$ and pristine TiO_2 after addition of coumarin. The emission spectra were registered using λ_{ex} = 350 nm.

Table S2. Comparison of photocatalytic activity of similar titanium dioxide-based catalyst in hydrogen evolution.

Photocatalyst	Co-catalyst amount(wt%)	Sacrificial electron donor	H_2 evolution (mmol/g*h)	Reference
$TiO_2/BP_{2.5wt\%}$	Pt (3%)	TEOA (10 vol%)	2.0	1
Mesocrystal TiO_2/Pt/BP NS	Pt (3%)	MeOH (25% vol)	9.1 (solar light, 2sun)	2
sea urchin-like TiO_2/BP QDs	-	MeOH (16.6% vol)	0.112 (UV-Vis)	3
$TiO_2/BP_{1\%}$	CoP(2%)	MeOH (20% vol)	7.4 (UV-Vis, 1.4 sun)	4
TiO_2/Cu_2O	-	MeOH (20% vol)	1.4 (Xenon lamp300W, no filter)	5
$P25/Cu_2O_{1.6\%}$	-	MeOH (10% vol)	10.5 (Filter AM 1.5)	6
$P25\text{-}V_0/Cu_2O_{1.5\%}$	-	MeOH (10% vol)	32.6 (Filter AM 1.5)	6
$P25/BP_{1\%}\text{-}Cu_2O_{5\%}$	-	MeOH (20% vol)	21.5 (Xenon lamp300W, no filter)	This work

Table S3. Extracted fitting parameters from the equivalent circuit fitting.

Photocatalyst	*R_1 (Ohm)*	*R_2 (Ohm)*	*R_3 (Ohm)*	*Q_2 [F.s^(a -1)]*	*Q_3 [F.s^(a -1)]*	*a_2*	*a_3*
TiO_2	9.31	6727.18	2404.44	65.74 ·10-6	4.50·10-4	0.91	0.99
Cu_2O	3.94	3319.12	777.03	1.50·10-4	6.39·10-3	0.93	0.68
Cu_2O-BP	7.67	1244.28	2201.21	2.77·10-4	3.00·10-4	0.93	0.84
TiO_2-BP	11.26	5004.23	2378.49	1.14·10-4	78.43·10-6	0.86	1.0
TiO_2-Cu_2O	4.78	930.70	348.27	1.62·10-3	3.16·10-4	0.89	0.93
TiO_2/Cu_2O-BP	6.29	200.62	889.18	2.31·10-4	1.81·10-3	0.92	0.65

Legend: R = resistance, Q = pseudocapacitance, a = exponent of the pseudocapacitance

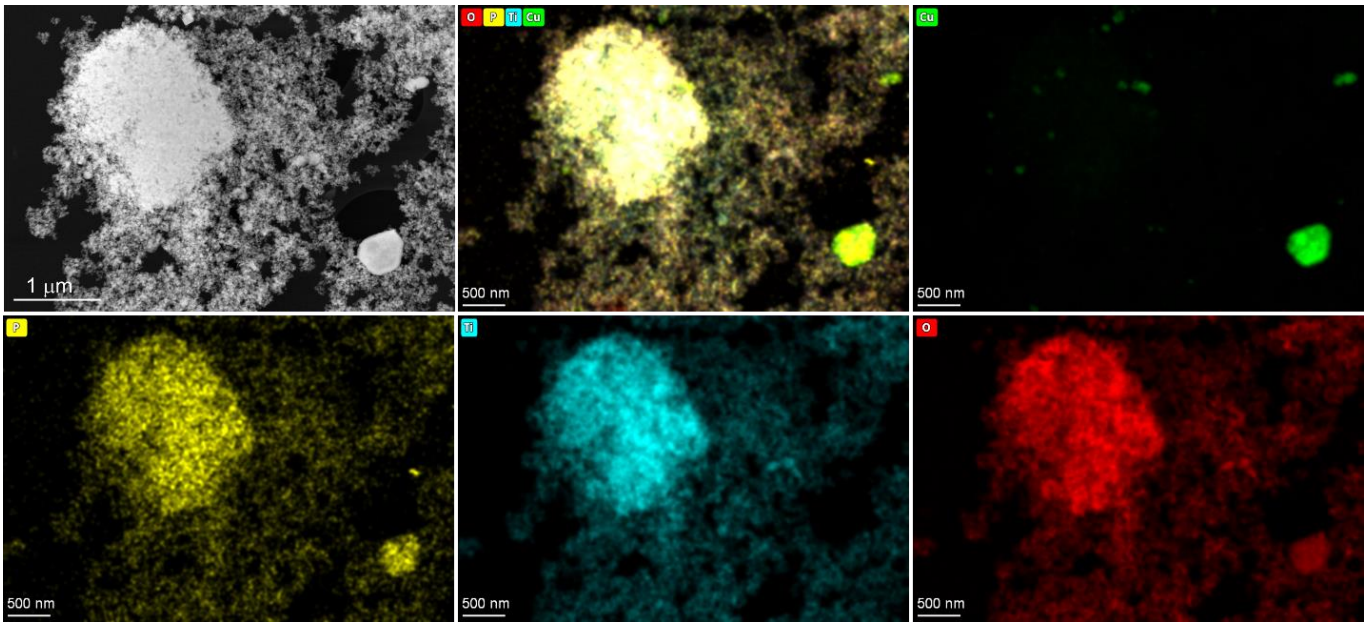

Figure S8. STEM HAADF image of TiO_2/(Cu_2O-BP)$_{6\%}$ recovered after photocatalytic tests, with the corresponding elements' distribution maps, obtained by EDX analysis.

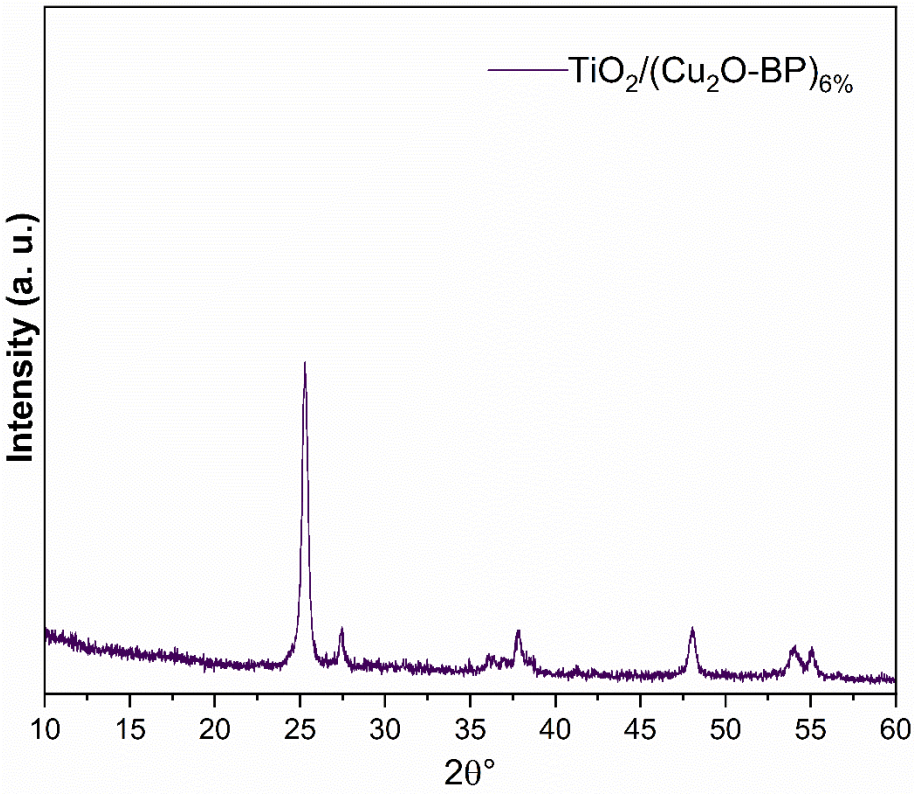

Figure S9. PXRD of $TiO_2/(Cu_2O\text{-}BP)_{6\%}$ recovered after photocatalytic tests.

Computational Chemistry Models

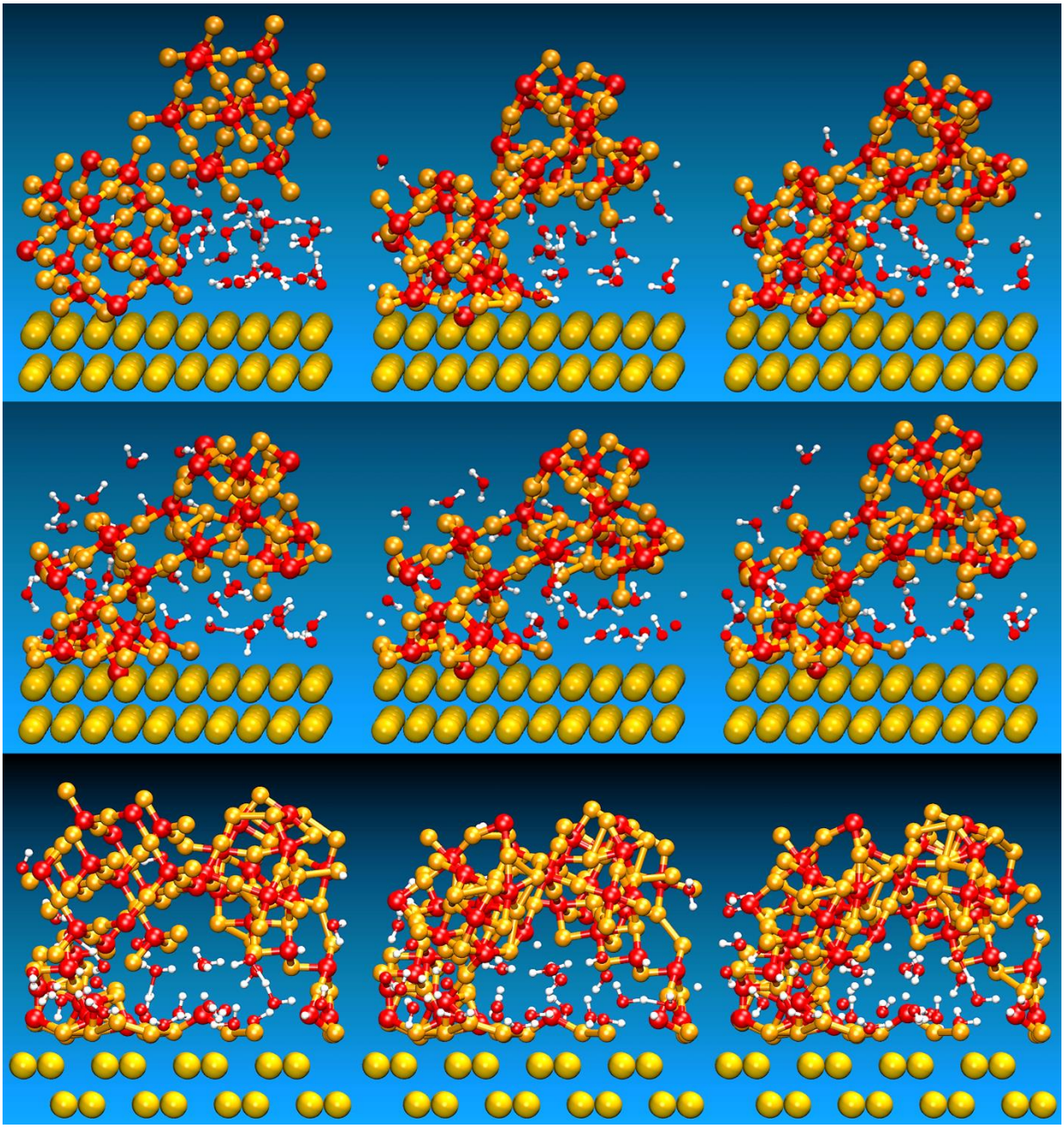

Figure S10. Preliminary models of the Cu_2O NPs growth process on a BP substrate partially covered with water molecules. The mechanism was simulated through ReaxFF MDs at low temperatures combined with structure optimization by progressively adsorbing small Cu_2O clusters on the BP surface. The clusters' aggregation determined the formation of the NPs, which remained slightly hydrated. BP is rendered by dark yellow spheres, whereas Cu_2O configurations are depicted with ball and stick representations (as water). Cu is orange, O red, and H white.

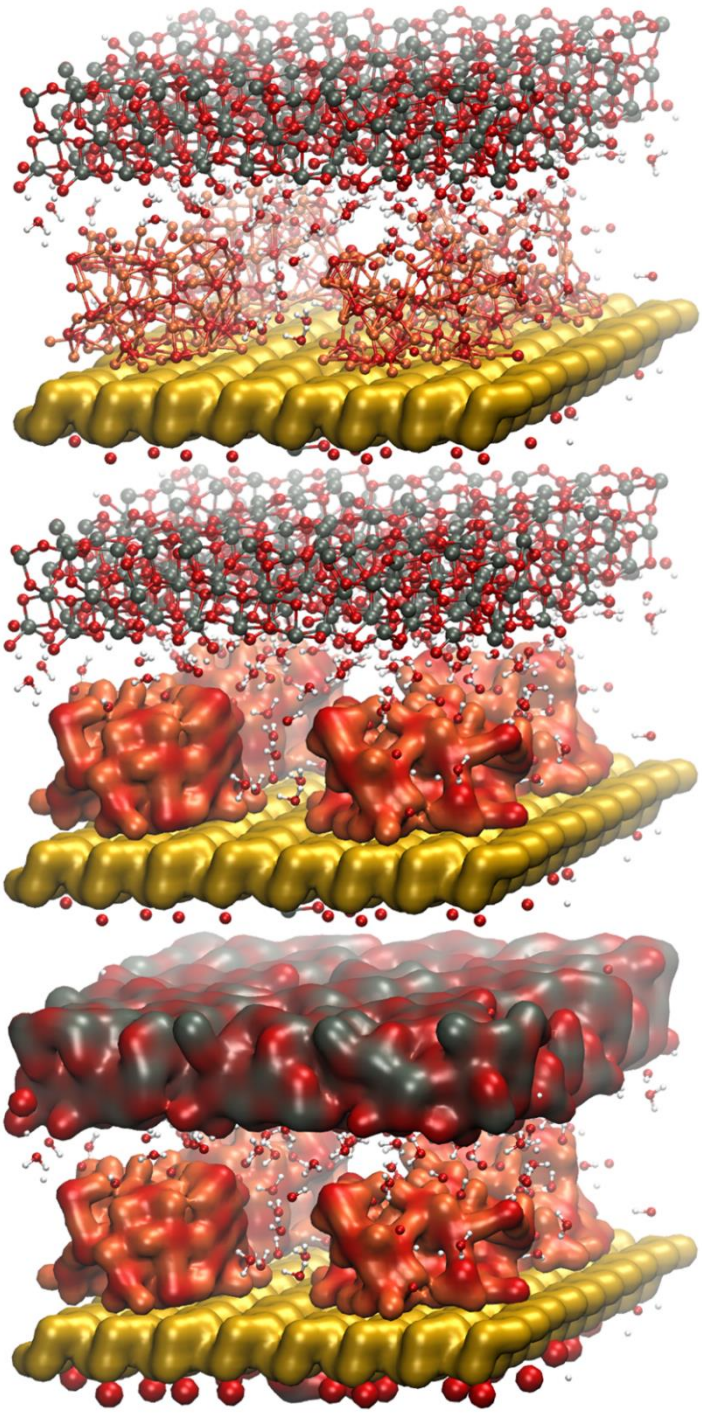

Figure S11. MD equilibrated model derived from the QM calculations by replicating 2x2 times the original optimized configuration. A few water molecules were included, optimized, and simulated in the NVT ensemble at ambient temperature for hundreds of picoseconds to test the system stability and force field performance. The BP support is rendered through a dark yellow solvent accessible surface (SAS); the four Cu_2O NPs and the anatase (TiO_2) slab are depicted by balls and sticks in the top and medium images, whereas in the bottom picture are both displayed as SASs to give an idea of the volume occupation. Color codes: P dark yellow, Cu orange, O red, Ti dark gray, H white.

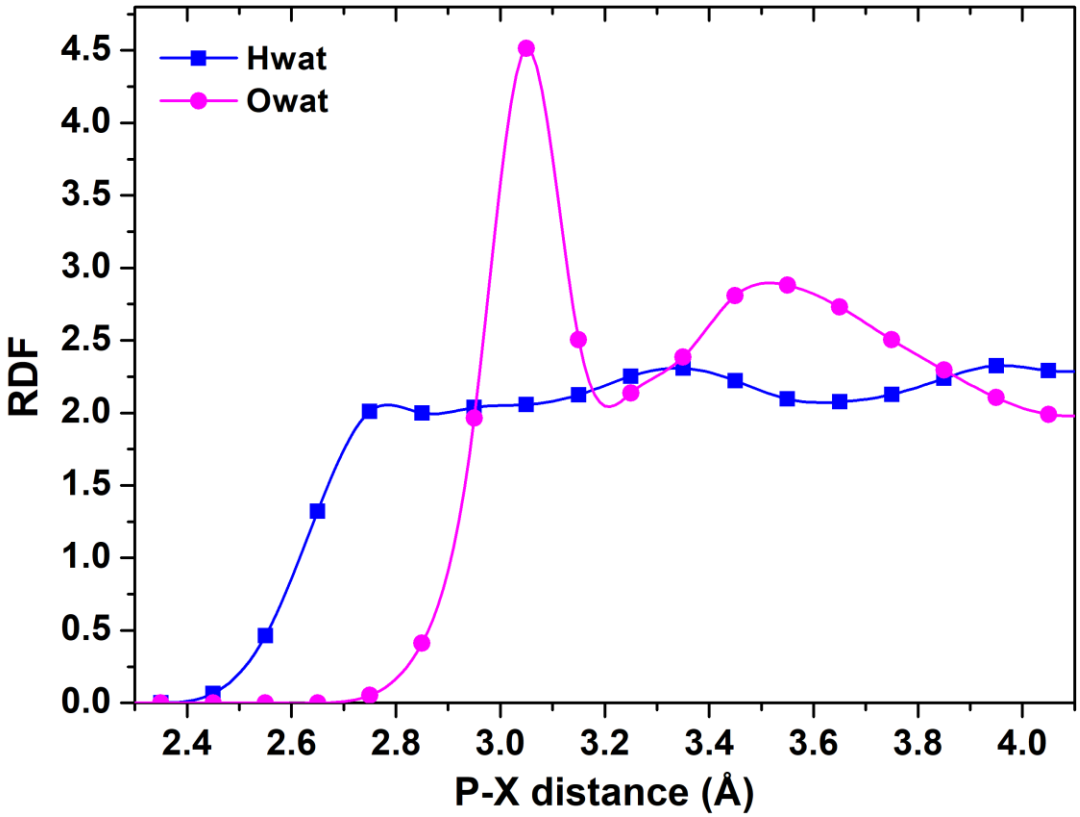

Figure S12. Atomic P-X radial distribution functions of the water molecules physisorbed on BP. The trends on the two plots confirm the hydrophobic nature of the BP-water interaction.

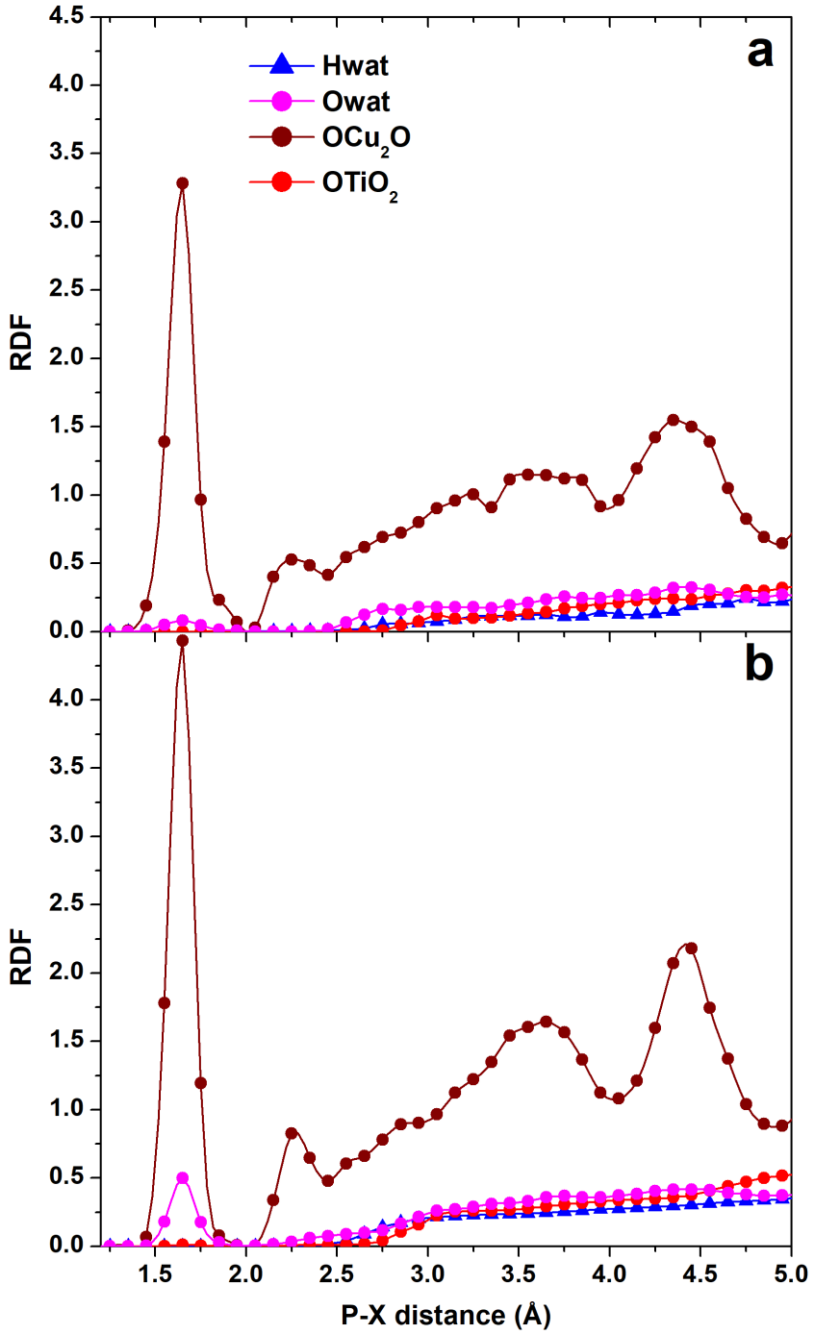

Figure S13. Atomic P-X radial distribution functions of the water molecules and oxide oxygens in TiO_2/BP-Cu_2O, calculated from the RMD trajectories at ambient temperature without perturbations (**a**), and when a constant electric field was applied to the system in the x direction (**b**).

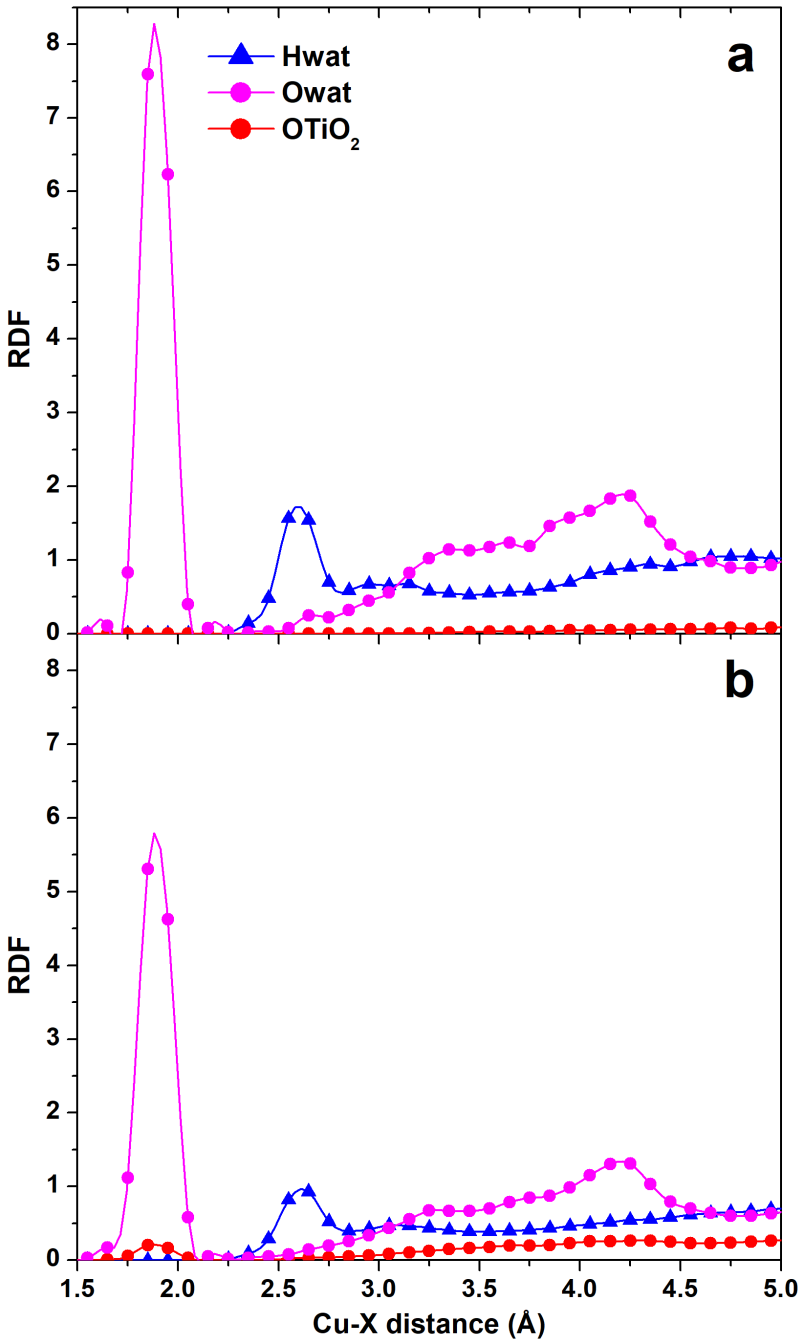

Figure S14. Atomic Cu-X radial distribution functions of the water molecules and oxide oxygens in TiO_2/BP-Cu_2O, calculated from the RMD trajectories at ambient temperature without perturbations (**a**), and when a constant electric field was applied to the system in the x direction (**b**).

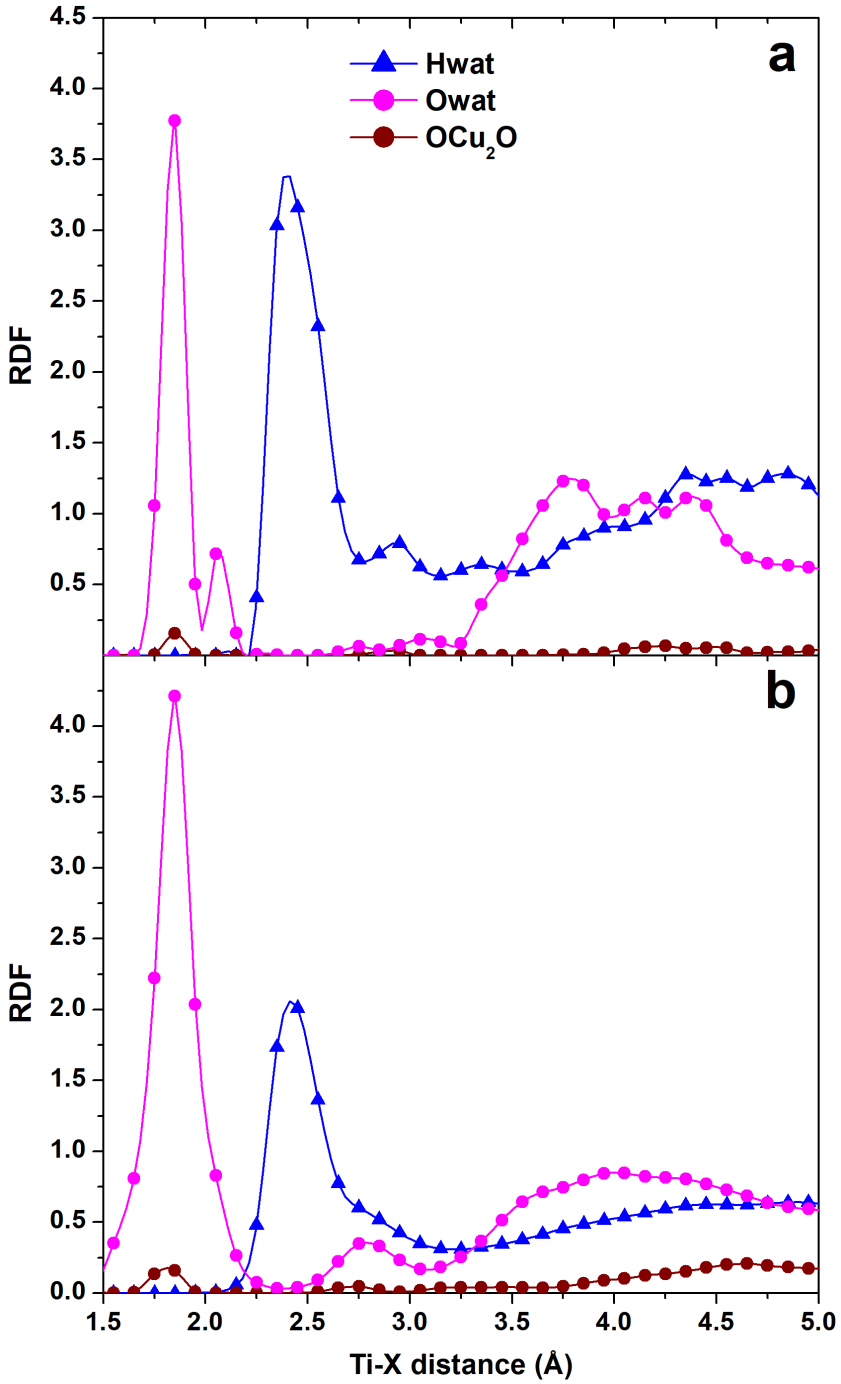

Figure S15. Atomic Ti-X radial distribution functions of the water molecules and oxide oxygens in the TiO_2/BP-Cu_2O composite material, calculated from the RMD trajectories at ambient temperature without perturbations (**a**), and when a constant electric field was applied to the system in the x direction (**b**).

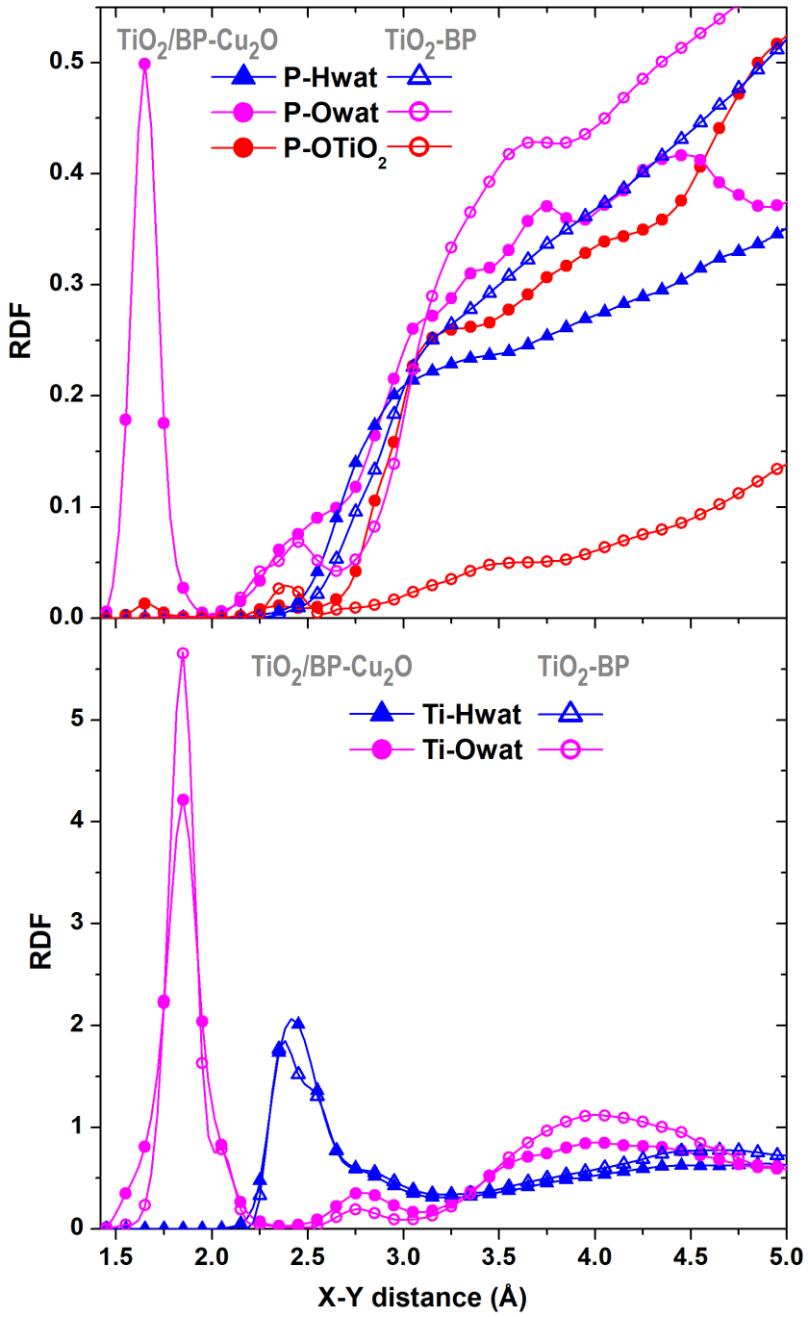

Figure S16. Atomic X-Y radial distribution functions of the water molecules and TiO_2 oxygens in the TiO_2/BP-Cu_2O and TiO_2-BP composite materials, calculated from the RMD trajectories at ambient temperature under the constant electric field perturbation.

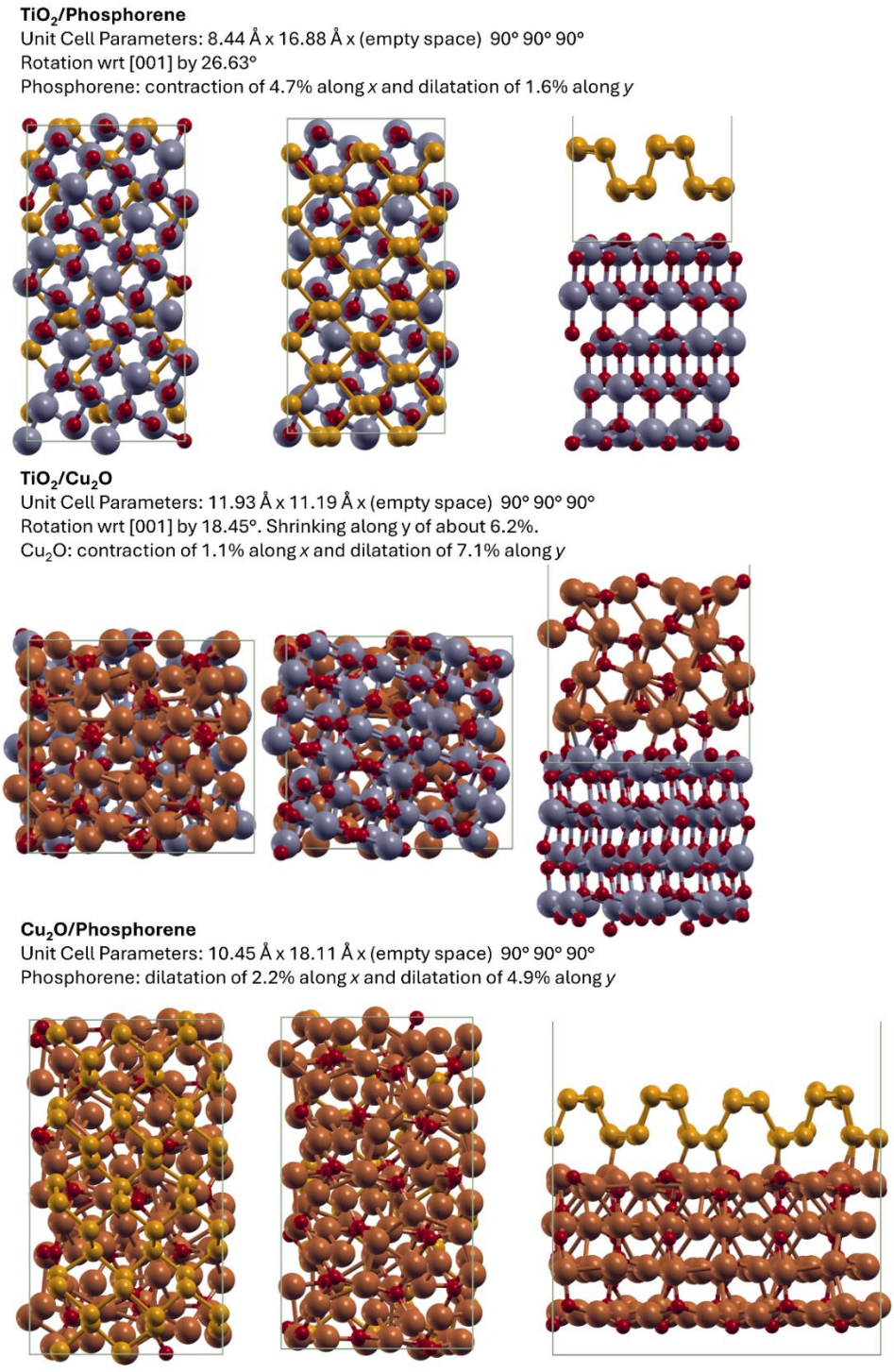

Figure S17. Unit cells developed to investigate the three individual interfaces, whose electronic structure is shown in **Fig. 8**. Color coding: Cu orange, O red, Ti gray and P yellow.

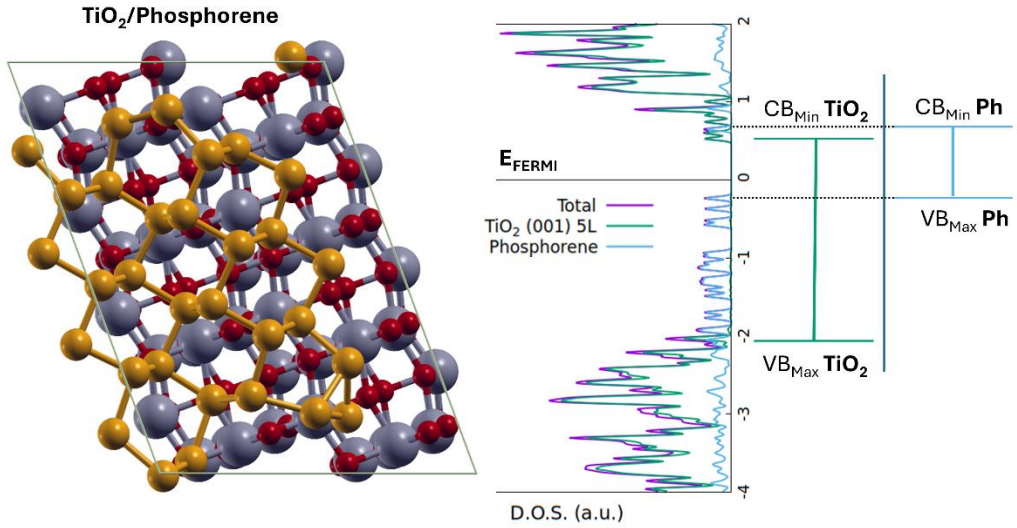

Figure S18. Unit cell, PDOS, and band scheme developed to investigate the interface between TiO_2(101) anatase surface and phosphorene. Color coding: O red, Ti gray, and P yellow.

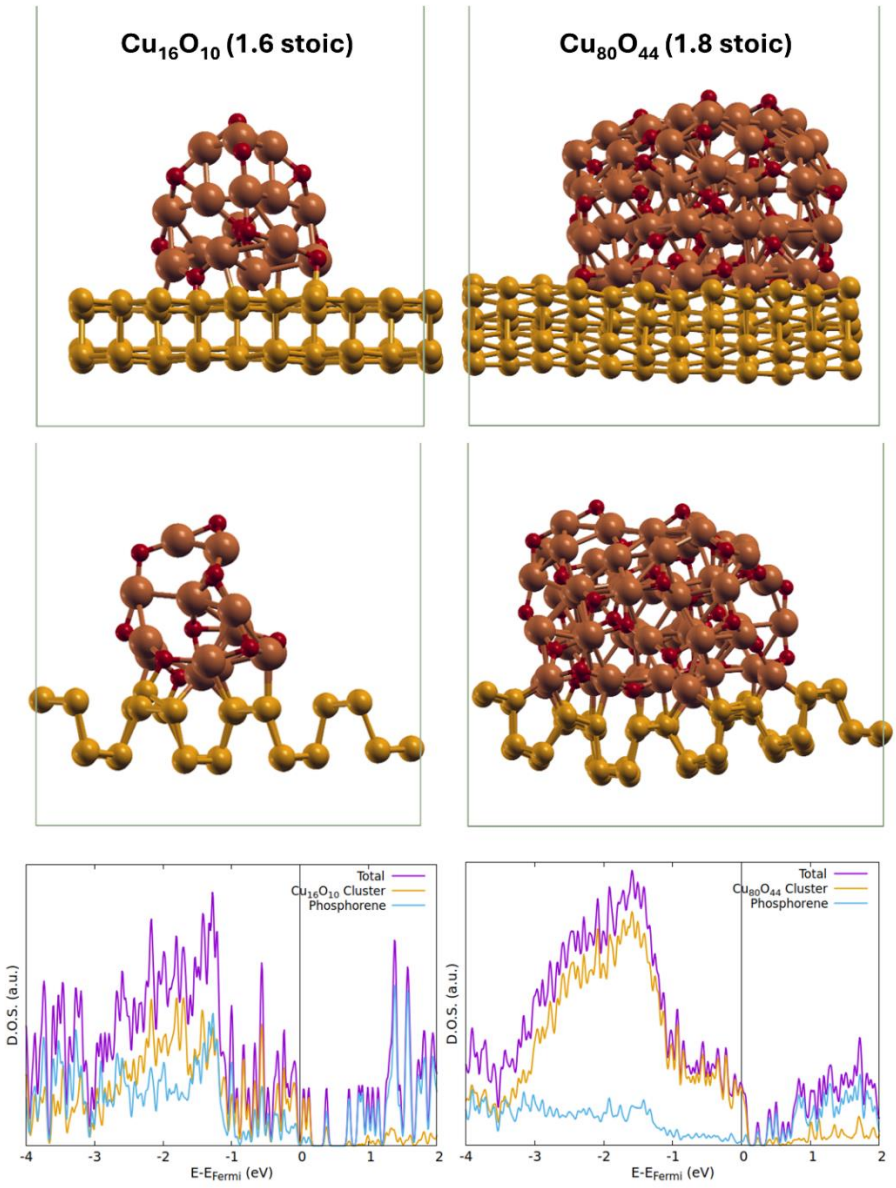

Figure S19. Unit cells and PDOS of two clusters deposited on Phosphorene. Color coding: Cu orange, O red, and P yellow.

We also tested the interaction between Cu_2O clusters and BP by considering a variety of structures derived by either a cutting of the Cu_2O bulk material or extracted from the RMD simulations. After local optimization, we observed the same strong coulombic interaction due to the charge transfer from interfacial P atoms to interfacial Cu/O atoms. The PDOS of these systems reveals the same intermixing of electronic states at the interface observed in the case of periodic epitaxy. Furthermore, the release of the periodic boundary conditions increased the possibility of structural rearrangement, showing a bending of the BP layer to maximize the interaction with the oxide.

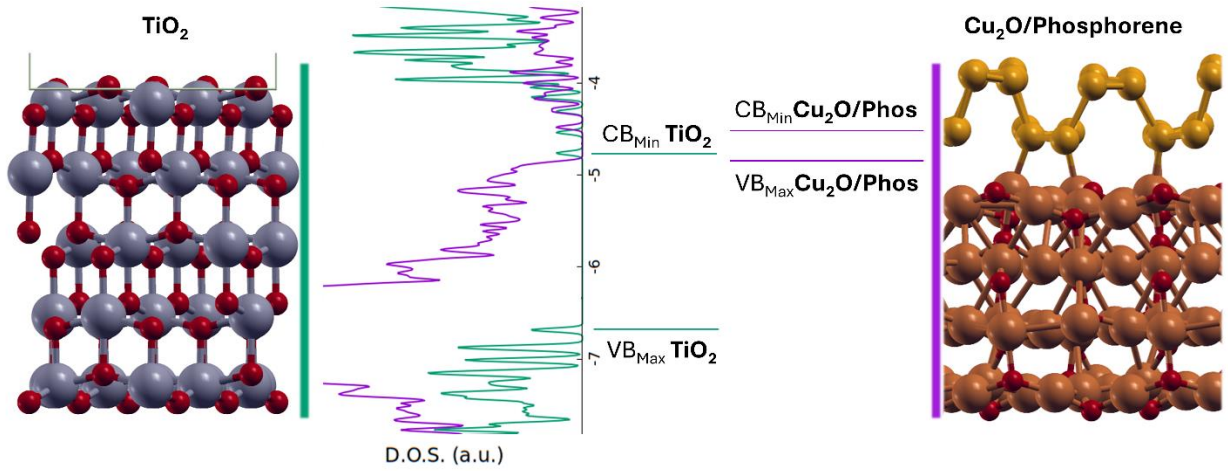

Figure S20. S-scheme corresponding to the investigated heterojunction. Left side: TiO_2 as the Oxidation Photocatalyst (OP), right side: the binary nanocomposite Cu_2O/Phos as the Reduction Photocatalyst (RP). Energies are in eV. Color atom coding: Cu orange, O red, Ti gray, and P yellow.

[1] Wu J, Huang S, Jin Z, Chen J, Hu L, Long Y, Lu J, Ruan S, Zeng YJ. Black phosphorus: an efficient co-catalyst for charge separation and enhanced photocatalytic hydrogen evolution. J. Mater. Sci. 2018;53:16557-16566. https://doi.org/10.1007/s10853-018-2830-2.

[2] Elbanna O, Zhu M, Fujitsuka M, Majima T. Black Phosphorus Sensitized TiO_2 Mesocrystal Photocatalyst for Hydrogen Evolution with Visible and Near-Infrared Light Irradiation. ACS Catal. 2019;9:3618-3626. https://pubs.acs.org/doi/10.1021/acscatal.8b05081

[3] Guan R, Wang L, Wang D, Li K, Tan H, Chen Y, Cheng X, Zhao Z, Shang Q, Sun Z. Boosting photocatalytic hydrogen production via enhanced exciton dissociation in black phosphorus quantum Dots/TiO_2 heterojunction. Chem. Eng. J. 2022;435:135138-135146. https://doi.org/10.1016/j.cej.2022.135138.

[4] Provinciali G, Filippi J, Lavacchi A, Caporali S, Banchelli M, Serrano-Ruiz M, Peruzzini M, Caporali M. Black Phosphorus as Promoter for Noble-Metal free Photocatalytic Hydrogen Production, ChemCatChem 2023;15:e202300647. https://doi.org/10.1002/cctc.202300647.

[5] Chen JL, Liu MM, Xie SY, Yue LJ, Gong FL, Chai KM, Zhang YH. Cu_2O-loaded TiO_2 heterojunction composites for enhanced photocatalytic H_2 production. J. Mol. Struct. 2022;1247:131294. https://doi.org/10.1016/j.molstruc.2021.131294.

[6] Wei T, Zhu YN, An X, Liu LM, Cao X, Liu H, Qu J. Defect Modulation of Z-Scheme TiO_2/Cu_2O Photocatalysts for Durable Water Splitting. ACS Catal. 2019;9:8346–8354. https://doi.org/10.1021/acscatal.9b01786.